LAWRENCE
LIVERMORE
NATIONAL
LABORATORY

LLNL-JRNL-852802

X-ray continuum spectroscopy of inertial confinement fusion implosions at the National Ignition Facility

S. Stoupin, A. G. MacPhee, B. Kozioziemski, M. J. MacDonald, N. Ose, J. M. Heinmiller, N. Izumi, D. Rusby, P. T. Springer, M. B. Schneider

August 4, 2023

Review of Scientific Instruments

Disclaimer

X-ray continuum spectroscopy of inertial confinement fusion implosions at the National Ignition Facility

S. Stoupin,[1, a)] A.G. MacPhee,[1] B. Kozioziemski,[1] M.J. MacDonald,[1] N. Ose,[1] J.M. Heinmiller,[2] N. Izumi,[1] D. Rusby,[1] P.T. Springer,[1] and M.B. Schneider[1]

[1)] *Lawrence Livermore National Laboratory, Livermore, CA 94550, USA*

[2)] *Nevada National Security Site, Livermore Operations, Livermore, CA 94550, USA*

A methodology for measuring x-ray continuum spectra of inertial confinement fusion (ICF) implosions is described. The method relies on the use of ConSpec, a high-throughput spectrometer using highly annealed pyrolytic graphite (HAPG) crystal [MacDonald et al. J. Instrum. 14, P12009 (2019)], which measures the spectra in $\simeq$ 20-30 keV range. Due to its conical shape the crystal is sagittally focusing a Bragg-reflected x-ray spectrum into a line, which enhances the recorded x-ray emission signal above the high neutron-induced background accompanying ICF implosions at the National Ignition Facility (NIF). To improve the overall measurement accuracy the sensitivity of the spectrometer measured in an off-line x-ray laboratory setting was revised. The error analysis was expanded to include the accuracy of the off-line measurements, the effect of the neutron-induced background as well as influence of possible errors in alignment of the instrument to the ICF target. We demonstrate how the improved methodology is applied in the analysis of ConSpec data with examples of a relatively low-neutron-yield implosion using a tritium-hydrogen-deuterium mix (THD) as a fuel and a high-yield deuterium-tritium (DT) implosion producing high level of the background. In both cases, the shape of the measured spectrum agrees with the exponentially decaying spectral shape of bremsstrahlung emission to within $\pm$ 10%. In the case of the high-yield DT experiment, non-monotonic deviations slightly exceeding the measurement uncertainties are observed and discussed.

I. INTRODUCTION

Measurement of x-ray emission in inertial confinement fusion (ICF) experiments is an important diagnostic approach aimed at better understanding of ICF performance. The spectral shape of the emitted continuum is related to the emission-weighted spatially-averaged electron temperature, which can serve as an integral characteristic of an ICF experiment. Approaches leading to physical interpretation of this apparent electron temperature have been discussed in the literature.[1,2] Cao et al.[1] derive that the electron temperature inferred from measurements of the x-ray continuum emission represents the emission-weighted, harmonic mean ($< 1/T_e >$) of the hot-spot distribution, averaged both spatially and temporally. Kagan et al.[2] predict influence of suprathermal electrons on the x-ray emission spectrum of the hot spot. A more complicated picture can emerge in analysis of high-yield implosions at NIF where distribution of electron temperatures in the target at the times of x-ray emission is inhomogeneous. Direct measurements of the continuum spectra are expected to constrain both simulations and data analyses in a variety of other diagnostic approaches relying on theoretical models.

Bremsstrahlung emission from an ICF target with a characteristic electron temperature T_e is expected to follow the spectral shape[3,4]

$$S(E) \propto e^{-\tau} \frac{e^{-E/T_e}}{E^{0.39}}. \quad (1)$$

The denominator in Eq. 1 originates from a fit to the opacity tables using atomic models by Scott and Hansen.[5] The optical depth $\tau \propto E^{-3}$ of the fuel and the remaining capsule shell at time of x-ray emission is considered to be negligible at photon energies above $\simeq$ 20 keV.

Measurements of x-ray emission using differential x-ray filtering spectrometers[3,4,6] enable inferences of T_e. Due to broadband x-ray response of the filters data analysis relies on the expected spectral shape (Eq. 1), which is well justified from the physics perspective. Nonetheless, measurements of the emission spectrum using a spectrometer with well-defined spectral response such as an x-ray diffracting crystal spectrometer are desired to provide direct assessment of the spectral shape. This aspect becomes increasingly important as ICF experiments enter the new regime of burning plasmas.[7–9]

In this work we demonstrate the applicability of the previously implemented continuum x-ray spectrometer (ConSpec)[10,11] to time-averaged measurements of x-ray emission from ICF implosions at the National Ignition Facility characterized by high (up to $\simeq 4 \times 10^{17}$) yields of 14.1 MeV neutrons. High throughput of the HAPG-based spectrometer and its sagittal focusing of the reflected x-ray spectrum to a line enable efficient discrimination of the x-ray signal above the baseline of very intense neutron-induced background recorded on image plates. Data analysis procedures are described for two indirectly-driven ICF experiments: shot N220220 using a mix of tritium, hydrogen and deuterium (THD) as the capsule fuel (neutron yield 4.33×10^{14}) and shot N220919 using a deuterium-tritium mix (DT) as the fuel (neutron yield 3.82×10^{17}). These two experiments reveal differ-

[a)] The author to whom correspondence may be addressed: stoupin1@llnl.gov

ent apparent T_e of ≃4 and 7 keV, respectively as well as very different levels of x-ray emission, where emission of the DT shot is ≃ 40-80 times brighter. The shapes of the measured experimental spectra agree with the spectral shape of Eq. 1 to within ± 10%. Non-monotonic discrepancies in the spectral shape are observed for the DT shot. These discrepancies exceed the estimated measurement uncertainties, which are at the level of ≃5% (r.m.s.). Analysis of the uncertainties presented in this work includes contributions due to errors in the spectrometer sensitivity which was measured off-line, errors due to spectrometer alignment in the NIF target chamber and noise in the neutron-induced background.

II. OVERVIEW OF THE SPECTROMETER

The continuum x-ray spectrometer (ConSpec) was designed and implemented at the NIF to measure x-ray emission in the 20-30 keV spectral range. To date ConSpec is the only high-throughput calibrated spectrometer at the NIF capable of measuring x-ray emission at energies above ≃ 20 keV." NSS (the NIF Survey Spectrometer) is another instrument which covers the energy range of interest, however, lacking the sensitivity to discern hard x-ray continuum in a variety of scenarios including high-yield ICF experiments. ConSpec and its main components are shown in Fig. 1(a). The front housing cone holds a polycarbon debris window. Radiation passing through this window is limited by an entrance aperture in front of the crystal. A line replaceable unit (LRU) holding this aperture can also include x-ray attenuating foils. The direct line-of-sight (LoS) from the source to the detector is shielded using a tungsten block combined with a step-down Cu-Al attenuator at the exit side of the block. The instrument is inserted into the NIF target chamber along the axis of the Diagnostic Instrument Manipulator (DIM axis), which makes an angle of 4.24° with the crystal spectrometer axis. The conical shape of the crystal is a key feature of the Hall geometry[12] where x rays reflected from the crystal are focused to a line that is perpendicular to the axis of the spectrometer. Such arrangement was implemented in ConSpec to explore future use of graphite conical crystals in combination with time-resolving detectors such as an x-ray streak camera.[13] Due to geometrical constrains of the NIF target chamber the streak camera photocathode must be normal to the DIM axis. ConSpec remains a time-integrating diagnostics where x rays reflected from the crystal are recorded on an image plate (IP) placed at normal orientation to the spectrometer axis at a distance of 900 mm from the ICF target (x-ray source). More details on the spectrometer components can be found in prior publications.[10,11]

The meridional (energy dispersing) and the sagittal (imaging) directions of the crystal are as shown by arrows in Fig. 1(b)). Figure 1(c) represents a ray-tracing diagram in the meridional midplane of the spectrometer.

TABLE I. Parameters of the spectrometer.

Reflection	E_b [keV]	E_0 [keV]	H [mm]	D [mm]
HAPG 002	1.8516	25.0	33.42	900.0

Assuming that over the small working section of the conical surface the rays approximately obey this diagram, the nominal dispersion law of the spectrometer can be approximated with that of a flat crystal:

$$x = D\tan\theta - 2H, \tag{2}$$

where D is the source-detector distance and $H = \frac{1}{2}D\tan\theta_0$ is the height of the source above the crystal, defined for the center Bragg angle θ_0, which corresponds to the center photon energy E_0. The Bragg's angle θ is related to photon energy via the Bragg's law:

$$E_b = E\sin\theta, \tag{3}$$

where $E_b = hc/2d$ is the Bragg's energy related to the d-spacing of the working crystal reflection d with h the Planck constant, and c the speed of light in vacuum. ConSpec is using the lowest reflection order HAPG 002 with Bragg angles in the range from ≃ 5.31° (20 keV) to 3.54° (30 keV). The key parameters of the spectrometer are summarized in Table I.

III. SPECTROMETER CALIBRATION. REVISED CRYSTAL SENSITIVITY.

X-ray calibration measurements were performed at the NIF x-ray optics calibration facility at LLNL[14] as detailed in a prior publication[11]. The measurement procedure can be briefly outlined as follows. The spectrometer was placed on a calibration fixture designed to replicate the working geometry on the NIF as shown in Fig.1(c). The axis of the instrument was defined using a pair of tungsten-wire crosshairs installed on the calibration fixture. A portable coordinate measurement machine (Faro Prime) was used to set the distance between the x-ray source and the crystal. The x-ray source was a microfocus-type (source size ≃ 15 μm) Truefocus TFX-8100 using Mo anode. The source was operated at a voltage of 65 kV. Spectra of the radiation reflected from the crystal were measured using an Amptek XR-100SDD Silicon Drift Detector (SDD) while scanning the detector along the spectral direction x in the detector plane. During the course of these measurements the x-ray tube current was 0.02 mA. The detector's count rate λ was kept at $\lesssim$ 50000 counts/s. The detector peaking time was $t = 2$ μs. The probability of a pile-up and the related undesired spectral distortion where two detected x-ray events are not discriminated can be estimated assuming Poisson statistics $P = \frac{1}{2}(\lambda t)^2\exp(-\lambda t) < 1$ %.

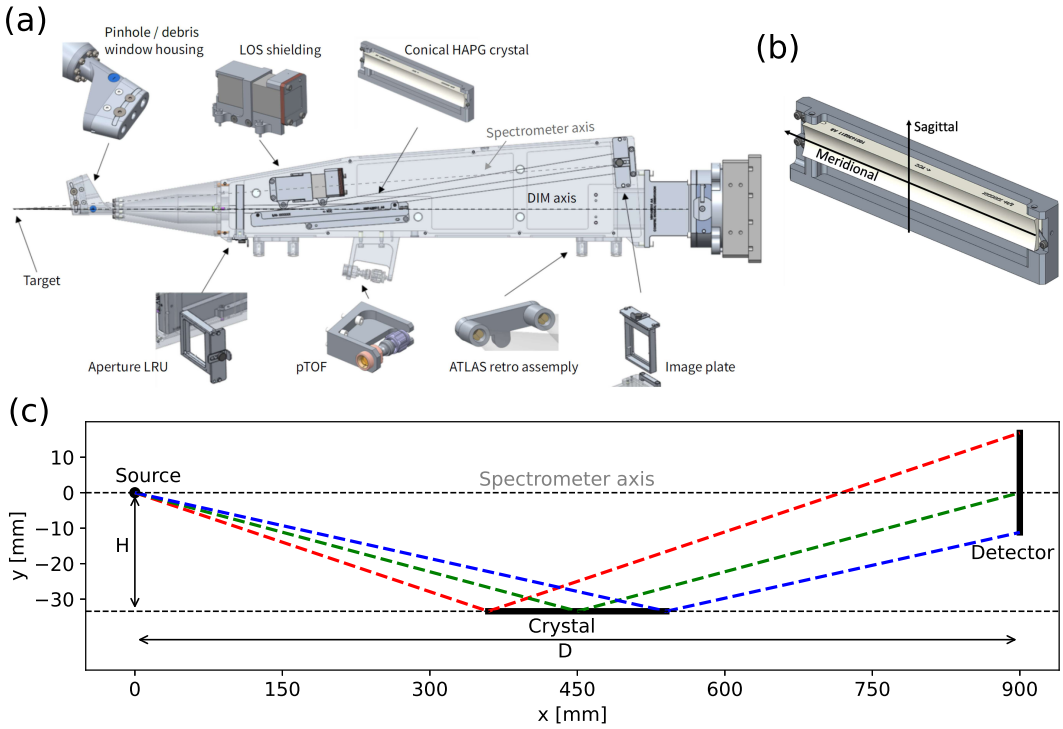

FIG. 1. (a) Layout of the ConSpec components. (b) Meridional and sagittal directions of the crystal. (c) Ray-tracing diagram of the spectrometer in the meridional midplane.

The measured spectra were scaled to 0.075 mA using a scale factor derived from measurements of the incident spectrum collected at both currents.

In this work improvements in determination of the crystal sensitivity function were implemented as follows. The spectrum of the x-ray source (operated at 65 kV, 0.075 mA) was measured in a separate calibration run by placing the Amptek SDD at a distance of 1883 mm from the source using a Ta pinhole collimator (pinhole diameter 400 μm). In order to limit spectral distortions caused by possible pile-up events the total count rate was $\lesssim$ 4000 counts/s. The measured spectrum is shown in Fig. 2(a). Unlike a similar measurement of the prior study[11] no K-edge attenuators were used. The newly measured spectrum was compared with the attenuation-corrected spectrum reported earlier. The spectra were found to be in agreement aside from minor discrepancies near the K-edge of the Ag attenuator (25.5 keV) used in the prior study.

The measured spectrum was fit to an empirical function $f(E) = \exp(\sum_{k=0}^{6} a_k E^k)$ in the range 20.3-60.0 keV. Figure 2(b) shows residuals obtained by subtraction of the fitted function from the measured spectrum binned to $\simeq 1/2$ of the Amptek's intrinsic energy resolution (250-300 eV). The standard deviation of the residuals in the range $\simeq$ 20-30 keV (shown in the Figure) is $\simeq$ 1%.

In the first step, collection efficiency of the crystal was calculated by dividing the reflected spectra by the measured incident spectrum in which the spectral intensity values above 20.3 keV were replaced with those of the fit. The intent of the incident spectrum fitting procedure described above was to eliminate a potentially harmful source of noise in the normalized data resulting from the division by the noisy signal). The collection efficiency as a colormap of normalized spectral values (in the units of μrad) is shown in Fig. 3(a) in the coordinates of detector's position x and its photon energy E_A. In this representation the full entrance aperture of the detector (diameter $\simeq$4.7 mm) was used in the measurements of the reflected x rays. The aperture size in energy units (1-2 keV) is a relatively large value if compared with the expected energy resolution of the crystal spectrometer ($\lesssim$ 200 eV). Hence to reduce the spectral blurring of the crystal response, differences were calculated between adjacent spectra measured in the detector scan. Figure 3(b) shows two adjacent spectra obtained at po-

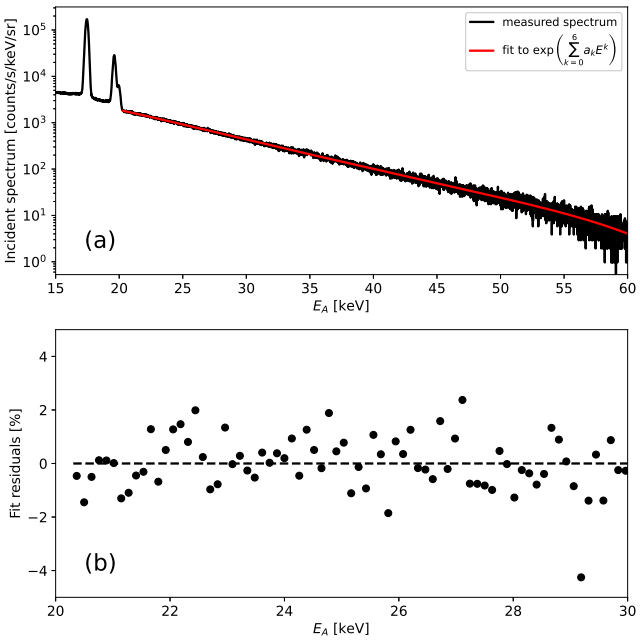

FIG. 2. (a) The incident spectrum measured using Amptek SDD (black) and a fit to $f(E) = \exp(\sum_{k=0}^{6} a_k E^k)$ (red) in the energy range 20.3-60keV. (b) Residuals obtained by subtraction of the fitted function from the measured spectrum binned to $\simeq 1/2$ of Amptek's intrinsic energy resolution (250-300 eV).

sitions x_i and x_{i+1} in the scan, while Fig. 3(c) shows the difference spectrum and its smoothed (Savitzky-Golay-filtered) representation. The collection efficiency can be alternatively defined using intensities of the peaks in the difference spectrum.[11] The positive peak corresponds to additional spectral intensity at the low energy (rising) edge of the spectrum gained in the spectrum upon shifting the detector to the new x_{i+1} position while the negative peak corresponds to the spectral intensity lost at the high energy (falling) edge. Thus, the peaks represent spectral intensities at the locations of the aperture edges over the distance intervals equal to the step size of the detector scan ($\Delta x = 0.1$ mm). Figure 3(d) shows the higher resolution collection efficiency derived using the intensity of the positive peak in units of [μrad/mm] (i.e., normalized by Δx).

In the second step, the dispersion relation of the spectrometer was derived from the energy positions of peak intensity for each value of the detector coordinate x. The positions were obtained by fitting the positive peak in the difference spectra to the Lorentzian shape. The positions were approximated with a third-order polynomial function as a function of x. The approximated dispersion is shown in Fig. 3(d) by the curved dashed line which overlaps with the contour of maximum intensity. The dispersion relationship derived from the positions of the positive peak was found to be compatible with the one derived from the positions of the negative peak as expected. The measured dispersion, its polynomial approximation (fit) and the nominal dispersion given by Eq. 2 are shown in Fig.4(a). The residuals obtained by subtraction of the approximations from the measured data are shown in Fig. 4(b). It can be seen that the polynomial approximation is preferable since the obtained residuals are smaller (contained within $\pm$ 0.05 keV unlike those of the nominal dispersion).

In the third step, sensitivity of the crystal in absolute units was calculated by integration of the collection efficiency along the detector-measured energy axis (E_A). The other dimension given by the detector coordinate x is transformed to the spectrometer's energy E using the dispersion relation. From Fig. 3 it can be seen that non-zero collection efficiency exists well beyond the reflection regime corresponding to the main Bragg reflection HAPG 002 (first-order). Additional contours of intensity are present as well as considerable noise. The second most intense contour corresponds to twice the energies of the first order reflection (i.e., second reflection order or HAPG 004). Double-photon counting by the detector (detector's pileup) may also contribute to the signal of this contour. Other weaker contours of intensity may be due to x-ray diffraction from in-plane misoriented domains of the HAPG crystal (i.e., a fraction of the Debye ring captured by the detector). The primary source of noise is division of the spectra (especially the noisy differential spectra) by the rapidly decaying incident spectrum (i.e., division by small numbers at higher energies). In order to isolate the sensitivity corresponding to the first reflection order (G_1), the integration of the high-resolution collection efficiency was performed in a limited spectral band around the contour of maximum intensity. The boundaries of the integration interval are shown in Fig. 3(d) by curved dashed lines offset form the contour of maximum intensity. This spectral filtering enabled rejection of the high-energy noise as well as higher reflection orders.

The first-order sensitivities derived from the positive and negative difference peaks (G_1^+ and G_1^-, respectively) were found to be slightly different as shown in Fig.5 (the shown quantities correspond to the integration band of 3.5 keV). This discrepancy can be due to non-equivalency of the two edges of the detector aperture in terms of x-ray intensity rejection (e.g., the edge being partially transparent to x rays). Also, because the choice of the integration band is somewhat arbitrary the band was varied in the interval 3.0-4.5 keV where for each chosen band values of crystal sensitivities G_1^+ and G_1^- were calculated. From the obtained set of crystal sensitivities the average sensitivity was calculated along with the standard deviation to represent uncertainty in determination of the first-order sensitivity. The averaged first-order crystal sensitivities are shown in Fig. 6 derived from the experimental data collected using two different apertures placed in front of the crystal which limit the footprint of the incident x rays on the crystal in the sagittal direction to 5 mm and 1 mm. The sensitivity corresponding to the

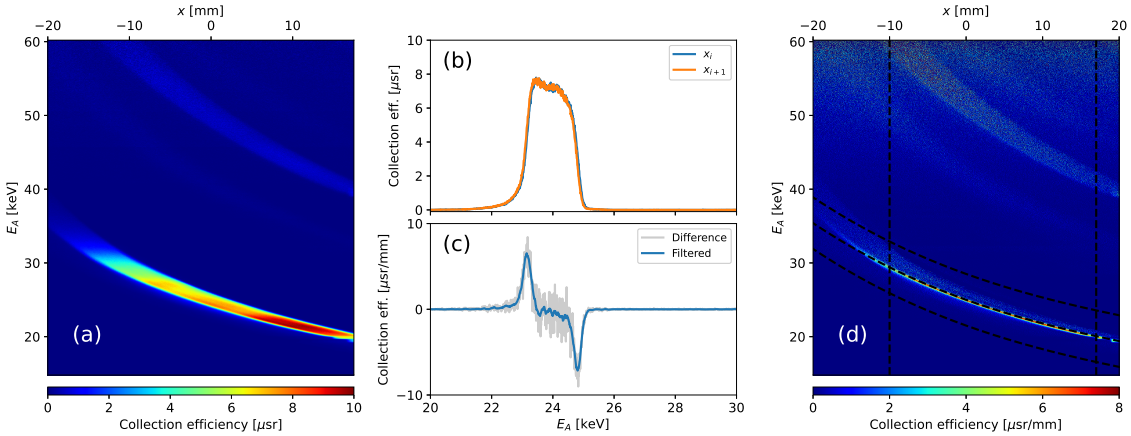

FIG. 3. (a) Collection efficiency of the HAPG crystal obtained using the spectra measured in the detector scan along the spectral direction x. (b) Two spectra in adjacent positions of the detector scan. (c) Difference signal as result of subtraction of the two adjacent spectra (original data and filtered for clarity). (d) High-resolution collection efficiency derived from the intensities of the positive peak of the difference spectra (a similar result for the negative peak is omitted for clarity). The curved dashed line overlapping with the contour of maximum intensity represents the dispersion of the crystal (fit in the range indicated by the two vertical lines). The curved dashed lines offset from the contour of maximum intensity indicate the boundaries of intervals where energy integration of the collection efficiency was performed to extract the first order crystal sensitivity.

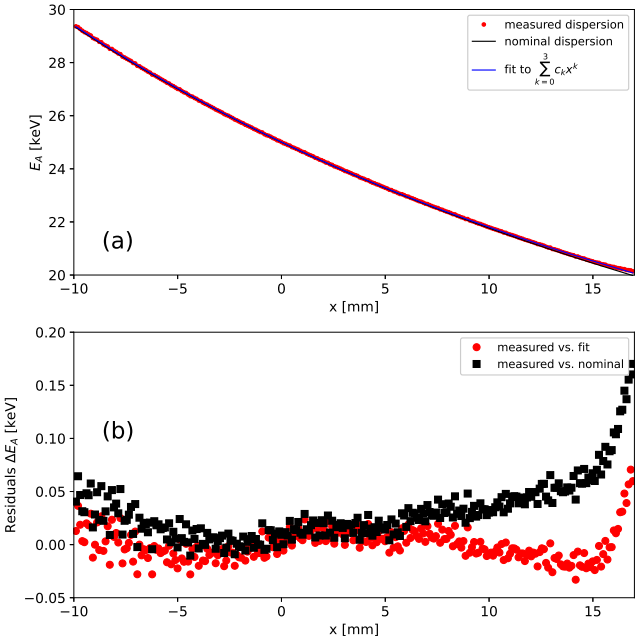

FIG. 4. (a) The measured dispersion obtained by fitting of the energy positions of peak intensity for each detector coordinate x (red circles). The nominal dispersion by Eq. 2 (black) and the third order polynomial fit (blue) to the measured dispersion. (b) Residuals obtained by subtraction of the approximations from the measured values.

1 mm aperture is scaled by factor of 5. It can be seen that the signal from the crystal is not exactly proportional to the illuminated width fraction of the crystal. This effect is likely due to geometric aberrations of the conical surface and a possible inhomogeneity of the crystal's mosaic where locally averaged orientation of the crystal lattice can deviate from the shape of the substrate.

In the final step, the second order sensitivity was estimated using and an integration procedure similar to the one described above for the first order sensitivity. Because the second reflection order is represented by much noisier signal in our measurements (weak source spectrum at 40-60 keV) the second order sensitivity was derived from the low-resolution collection efficiency (Fig.3(a)). The low-resolution first order and second order crystal sensitivities W_1 and W_2 were calculated by integration in a limited band around their corresponding contours of maximum intensity. They are shown in Fig.5 normalized by the diameter of the detector aperture. In this representation the second order sensitivity W_2 is shown as function of the primary photon energy (20-30 keV). The high-resolution second order sensitivity can be estimated as $G_2 = G_1 W_2/W_1$. The estimate is shown in Fig. 6 derived from data collected using the 5 mm aperture.

IV. ATTENUATORS. SIGNAL DETECTION.

In the analysis of x-ray spectra emitted by the indirectly-driven ICF target additional x-ray attenuation is related to transmission of a diagnostic window in the hohlraum wall.[15] The window is a $\simeq 160$ μm-thick block of synthetic diamond (high-density carbo, HDC) coated with 2.25 μm of Au. The x-ray transmission of the window is dominated by that of the Au film and is included in the data analysis of ConSpec as the first attenuating element. The second element is the polycarbonate debris

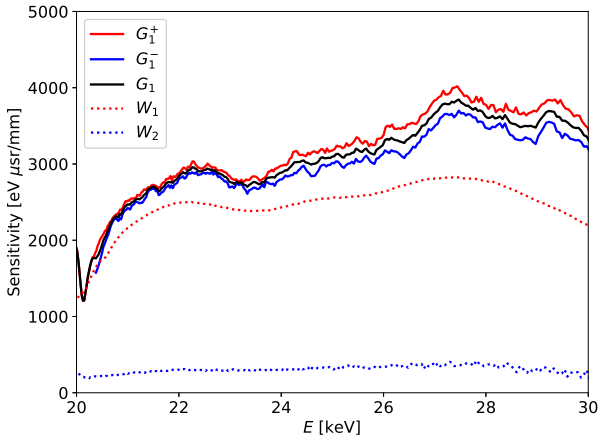

FIG. 5. The first-order crystal sensitivities derived from the positive and negative difference peaks G_1^+ and G_1^-, respectively) and the average of the two G_1. Savitzky-Golay-filtered values of G_1^+, G_1^- and G_1 are shown for clarity. The first and the second order sensitivities W_1 and W_2 derived from the low-resolution collection efficiency (Fig.3(a)).

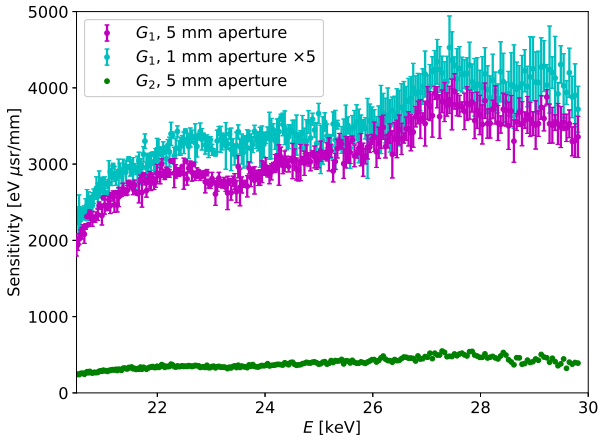

FIG. 6. The averaged first-order crystal sensitivities G_1 calculated from data collected using the crystal's limiting entrance aperture of size 5mm and 1mm (no filtering or binning applied). The error bars illustrate the uncertainties (± standard deviation). An estimate for the second order sensitivity $G_2 = G_1 W_2/W_1$ is shown obtained using the low-resolution data collected with 5 mm aperture.

shield which consists of the primary 2-mm-thick polycarbon insert and optional extra 1 mm-thick polycarbon inserts which provide additional protection to the downstream components of the spectrometer.

The aperture LRU contains a configurable set of metal foil attenuators. These attenuators can provide an energy reference in the spectrum (e.g., In foil with K-edge absorption at ≃28 keV) and/or attenuate predominantly the strong low-energy portion of the spectrum in order to approximately equalize the signal on the IP. This equalization is performed for high-yield experiments with substantial levels of x-ray emission to avoid possible distortion of the signal due to exceeding the onset of intrinsic saturation of the image plate. The image plates used in ConSpec spectrometer are Fuji SR-type. They are scanned at 24-hour after exposure with 25×25 μm^2 resolution. The scanned images are corrected for the fade effect. We estimate the onset of IP saturation to be at ≃8000 PSL per 25×25 μm^2 resolution element for volumetric excitation of 20-30 keV x rays based on extrapolation of data reported for 8 keV x rays by Templer et al.[16] For an x-ray spectrum with an apparent $T_e \simeq 7$ keV, such attenuation is accomplished using Ti foils with combined thickness of $\simeq$ 350 μm. For any given experiment the level of x-ray emission can vary by orders of magnitude depending on ICF performance. In order to avoid exceeding the dynamic range of the image plate scanner, calibrated neutral density filters with different optical densities are used to attenuate the measured photostimulated emission from the IP during the scan. The optical density of the filters is chosen based on the neutron yield of the target. To further mitigate the potential outcome of distorted/clipped images, we take advantage of the semi-transparency of the IPs to 20-30 keV x rays. A second IP is used to record the x-ray signal transmitted through the first IP. Thus, the first plate serves as transmission-mode x-ray detector. It does attenuate the incident x rays substantially, hence we calibrated the spectral transmission and x-ray fluorescence of the IPs. Measurements of x-ray transmission for the attenuators used in the spectrometer were performed at Nevada National Security Site (NNSS) using an x-ray source which offered a selection of energies of characteristic emission in the range 20-30 keV. For each attenuator measurements were performed over a central 10×10 mm area on a 5×5 grid using an x-ray beam with a spot size of $\simeq$ 2mm (diameter). The combined accuracy of these measurements was better than 1% (confidence interval). X-ray transmission measurements of ConSpec's IPs were also performed on individual basis for selected ICF experiments at the NIF. For two selected image plates the transmission measurements were extended to 60 keV to evaluate IP transmission for the second reflection order of the HAPG crystal. The averaged experimental x-ray transmission data were found to be in good agreement with results of Maddox et al.[17]

The levels of x-ray fluorescence generated during absorption of 20-30 keV x rays and emitted from the back side of the plates were accessed in separate experiments where spectra of radiation transmitted through the IP were measured using a Ge energy-discriminating detector placed at the minimal possible sample-detector distance. These spectra were normalized by the transmitted level of the primary excitation. The resulting normalized fluorescence levels were scaled with a factor representing the ratio of half-space solid angle 2π to the actual collection solid angle at that minimal distance. Several characteristic lines as primary excitations were tested in the range

$\simeq$ 20-60 keV. The only substantial contribution $\simeq$ 5% was found for Fe K-α lines emitted from the magnetic layer of IP. To suppress this emission to a negligible level a buffer layer of 100-300 μm-thick Al combined with a darkened 25 μm-thick kapton sheet was used in between the two image plates in the stack. Several other lines were identified in the transmission spectra which were consistent with the elemental composition of the image plate. Their solid-angle-rescaled relative fluorescence levels were found to be $\lesssim$ 1%.

V. SPECTROMETER'S RESPONSE. INFLUENCE OF HIGHER CRYSTAL REFLECTION ORDERS.

The spectral signal $M(E)$ [PSL/mm] extracted from the image plate (where PSL are units of photostimulated luminescence) can be related to the incident x-ray spectrum $S(E)$ [mJ/keV/sr], the first and the second order crystal's sensitivities $G(E)$, the image plate sensitivity $I(E)$ [PSL/photon] and the combined transmission of spectrometer's attenuators $F(E)$.

$$M(E) = I_1F_1G_1S_1 + I_2F_2G_2S_2 \quad (4)$$

The indicies in the above relation indicate that the quantities (as functions of the photon energy) were evaluated in the primary energy range of the spectrometer covered with the first-order Bragg reflection (index 1) and in the range of energies corresponding to the second-order reflection (index 2). Higher reflection orders from the crystal are neglected due to rapid reduction of the spectral intensity at higher energies. Other contributions to the image which include incoherent scattering of x rays from the crystal, its substrate and other components of the spectrometer result in a nearly uniform background on the image plate which is subtracted from the image prior to extraction of $M(E)$.

It is of interest to evaluate the two terms of Eq. 4 independently in order to identify scenarios where the contribution of the second order becomes non-negligible. Figure 7(a) shows the ratio of the two crystal sensitivities G_2/G_1 and the ratio of the corresponding spectrometer responses $\tilde{G}_2/\tilde{G}_1 = I_2F_2G_2/(I_1F_1G_1)$ which is the quantity proportional to the ratio of the signals due to the second and the first order reflections recorded on the image plate. Unlike the ratio of the sensitivities, the ratio of the spectrometer's responses $\tilde{G}_2/\tilde{G}_1$ is increased substantially at lower photon energies where transmission of the first order is suppressed relative to that of the second order while the ratio of image plate sensitivities evaluated separately for the two energy intervals is about 1.[18] Hence, enhancement in the signal due to the second order reflection is expected at lower energies which could change the apparent slope of the continuum spectrum. Figures 7(b,c,d) show the expected image plate signals by Eq. 4 using trial incident spectra of Eq. 1 with values of T_e = 5,7,10 keV, respectively. The signal due to the first and second order spectrometer response are shown separately as well as their sum. In addition, the sum combined with a randomly generated noise of 5 % is shown. It is used to simulate determination of the apparent temperature (T_e') in a practical scenario. For each of the three spectra the noise was randomly generated in 1000 trials. In each trial the obtained noisy signal M' was converted to its spectral representation using the first order response only $S' = M'/\tilde{G}_1$, and a fit to Eq.1 in the range 20.7-29.5 keV was performed to determine the apparent temperature. Table II shows the apparent T_e' calculated as the mean value of the temperatures determined in the trials along with the standard deviation. A similar procedure was performed for an arrangement where an additional attenuator with x-ray transmission of the image plate is used. This situation corresponds to the signal extracted from an extra image plate placed behind the primary one (i.e., second plate in the stack). It is expected that the extra plate will further attenuate the signal due to the first order relative to the signal due to the second order, which will result in increased mismatch between T_e' and T_e. The extracted T_e' for these two scenarios (IP_1 and IP_2) are summarized in the table. The mismatch presents itself as reduction in the apparent temperature with respect to the nominal T_e, which is understood based on a slight boost in the spectral signal at lower photon energies due to the second order response. The mismatch is quite small ($\lesssim$ 1 % for IP_1, $\lesssim$ 3 % for IP_2) for conditions encountered so far in high-yield ICF implosions at the NIF ($T_e' \simeq$ 5-8 keV). However, the second order correction should be considered in those outcomes of ICF experiments where the apparent temperature becomes greater, especially in scenarios when readout of signal from IP_1 fails (e.g., due to saturation/clipping effects) and the spectral intensity is derived from IP_2.

TABLE II. Results of simulations where a spectrum $S(E) \propto e^{-E/T_e}E^{-0.39}$, using nominal T_e = 5,7,10 keV was propagated through the spectrometer's response given by $\tilde{G}_1$ and $\tilde{G}_2$ and combined with 5% r.m.s. noise to obtain signals recorded on the first (IP_1) and second (IP_2) image plates in the stack. The resulting noisy signals were converted back to the spectral representation using only the first-order response $\tilde{G}_1$. The resulting spectra were fit to Eq.1 to extract the apparent values T_e'. The values in brackets represent standard deviation of 1000 trials of random noise generation.

T_e [keV]	T_e' IP_1 [keV]	T_e' IP_2 [keV]
5.0	4.98(0.04)	4.96(0.10)
7.0	6.93(0.12)	6.81(0.19)
10.0	9.68(0.19)	9.10(0.34)

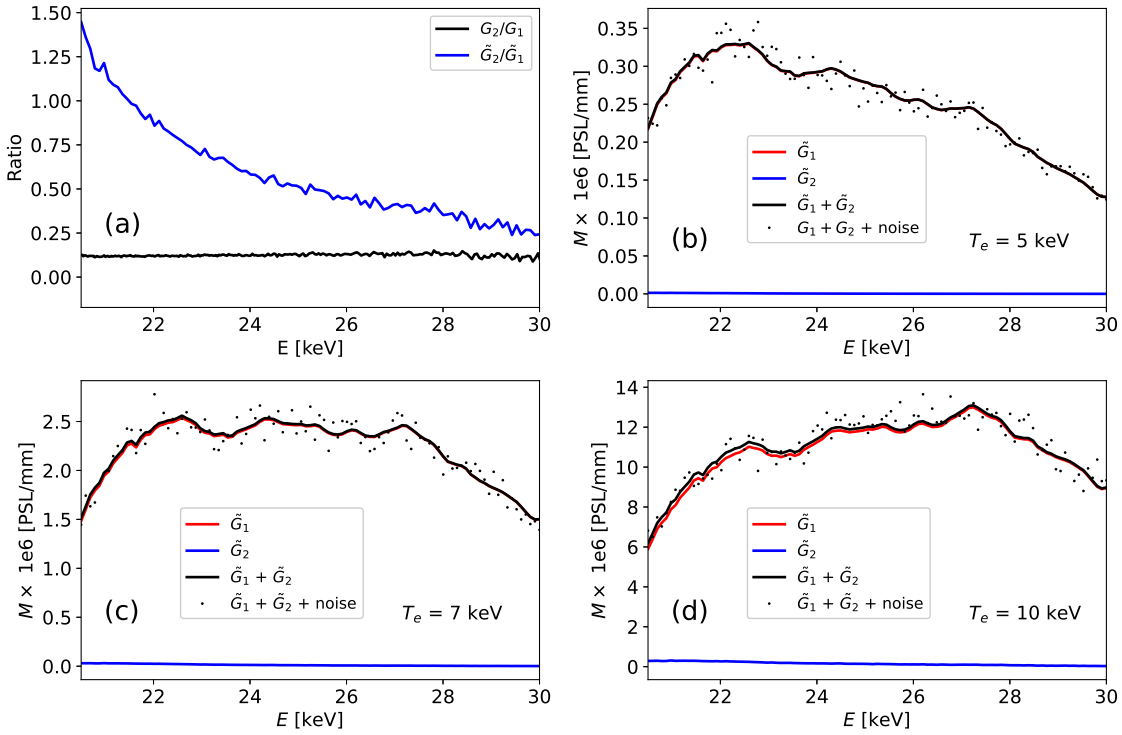

FIG. 7. (a) The ratio of the crystal sensitivities (G_1 is due to the first/primary reflection HAPG 002 and G_2 is due to HAPG 004) along with the ratio of the corresponding spectrometer responses ($\tilde{G}_n = I_n F_n G_n$, where I_n is the sensitivity of the image plate and F_n is the transmission of spectrometer's attenuators. (b-d) Simulated signals on the image plate for incident spectra $S(E) \propto e^{-E/T_e} E^{-0.39}$, T_e = 5,7,10 keV, respectively. The signals due to the first and the second order response are shown separately as well as their sum and the sum affected by 5% r.m.s. randomly generated noise.

VI. CORRECTIONS DUE TO ERRORS IN ALIGNMENT OF THE SPECTROMETER

In each ICF experiment the spectrometer is uniquely aligned to the x-ray emitting target using the advanced tracking laser alignment system (ATLAS). The accuracy of this alignment for ConSpec is specified as ± 2 mm insertion error (error in placement of the spectrometer along the DIM-axis) and ± 0.5 mm error in spectrometer pointing on the target (deviations in the two orthogonal directions). The values of these errors represent confidence intervals. These errors can lead to changes in the spectrometer response which will ultimately affect the measurement results. In addition, the errors in alignment of the NIF laser beams to the target will similarly affect the location of the x-ray source with respect to the spectrometer. These errors, however, are considerably smaller, limited to ± 50 μm r.m.s.[19] Consideration of the alignment errors and development of appropriate corrections are required for accurate spectroscopic measurements.

Let us consider, for simplicity, pointing and insertion errors with respect to the spectrometer axis. The pointing and insertion errors with respect to the DIM-axis are practically equivalent due to the small angular offset between the two axes. Figure 8 illustrates the ray-tracing scheme in the meridional midplane of the spectrometer where the x-ray source (red circle) was shifted with respect to its nominal location (black circle). We neglect the influence of the pointing error in the direction perpendicular to the plane of the drawing. Since for ConSpec $\sin\theta \simeq \theta$, this error results only in a negligibly small correction to the incidence angle θ, on order of $\theta(1-\cos\phi)$, where $\phi \simeq 1$ mrad is the angular deviation of the source in the out-of-plane direction. Thus, the photon energy of the reflected x rays defined by the angle θ remains unaffected by ϕ.

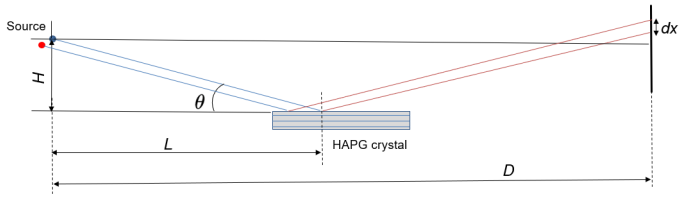

FIG. 8. Schematic of the spectrometer in the meridional midplane illustrating the effect of pointing and insertion errors.

The remaining two errors are δH, the variation of the source height above the crystal and δL, the variation of

the spectrometer insertion distance. In the spectrometer coordinates these errors correspond to a shift in the source position. An incident ray which makes an angle θ with the HAPG (002) crystal planes is offset by a certain amount along the crystal. It strikes a different location on the crystal which may have a distinct x-ray reflectivity due to inhomogeneous character of HAPG crystal lattice. This effect can be taken into account in the original sensitivity $G_1(E)$ by shifting the energy scale., i.e. using a corrected sensitivity $G_1'(E) = G_1(E + \delta E)$. Considering smallness of the deflections δH and δL the change in the angle θ for a given location L on the crystal is obtained using differentiation of the flat-crystal relation $\tan\theta = H/L$:

$$\delta\theta = \cos^2\theta\Big(\frac{\delta H}{L} - \frac{H\delta L}{L^2}\Big) \tag{5}$$

The corresponding offset in the energy scale δE is obtained using differential form of the Bragg's law $\delta E/E = -\delta\theta/\tan\theta$. For ConSpec $\tan\theta \simeq \sin\theta \simeq \theta$. This approximation leads to a simple form of the energy scale correction:

$$\delta E = -\delta H\frac{E}{H} + \delta L\frac{Eb}{H} \tag{6}$$

While this correction assigns correct energies to the crystal's sensitivity it is incomplete as it does not show where these energies are projected on the detector. The modified dispersion relationship is

$$x' = (D + \delta L)\tan\theta - 2H - \delta H \tag{7}$$

Comparing with the original dispersion relation Eq.2, rays corresponding to energy E will shift on the detector by

$$\delta x = \delta L\frac{E_b}{E} - \delta H. \tag{8}$$

Here we used the approximation of small Bragg angles for ConSpec $\tan\theta \simeq E_b/E$. It should be noted that the shift is approximately constant for all energies, since $E_b \lesssim 10E$ for ConSpec. Thus, the dispersion relationship of a misaligned spectrometer can be established unequivocally by assignment of position of a spectral reference (e.g. fluorescence line or an absorption edge of an attenuator) to the relevant photon energy per the original dispersion relation. However, the above derivations suggest that in a general case this approach should be considered as an approximation.

Several simulations are described below to explore and justify these corrections. We note that the corrections were formulated analytically using the nominal dispersion of the flat crystal, which is an approximation. As illustrated in Fig. 4 the polynomial fit provides better agreement with the measured dispersion. Hence, in the first step we explore the extent to which the nominal dispersion is applicable. In the simulations the polynomial fit represents the true spectrometer dispersion while the consequence of using the nominal dispersion as an approximation is explored. Figure 9(a) shows a signal recorded on an image plate which corresponds to a spectrum $S_0(E)$ by Eq.1 where τ=0 and T_e = 7.3 keV. The spectrum was forward propagated through the spectrometer response $\tilde{G}_1(E)$ using the measured original crystal sensitivity $G_1(E)$ and projected on the image plate using the dispersion given by the polynomial fit (labeled $M_p(x)[G_1(E)]$) and the nominal dispersion (labeled $M_n(x)[G_1(E)]$). A slight discrepancy is observed at values of x corresponding to the low photon energies. This discrepancy is also seen in the spectral representation of the two signals shown in Figure 9(b) where the original spectrum $S_0(E)$ is compared with a spectrum recovered from $M_n(x)[G_1(E)]$ using the polynomial dispersion approximation (the spectrum is labeled $S_p(E)[M_n]$). The difference between the two spectra is shown in Figure 9(c) as residuals [%]. The discrepancy between the two spectra remains to be low in practical terms ($\lesssim 2\%$) for energies $E \gtrsim 21\ keV$.

In the second step, we assume a misaligned spectrometer using the most extreme values of δH = -0.5 mm and δL = 2.0 mm, which taken together result in the worst possible reduction of the nominal θ angles that the incident rays make with the reflecting crystal planes. The corrected crystal sensitivity $G_1'(E) = G_1(E + \delta E)$ and the modified dispersion relation Eq. 7 are used to generate the detector's signal $M_n'(x)[G_1'(E)]$. This signal along with the original $M_p(x)$ are plotted in Fig. 9(d). We note that the shapes of the two signals are not exactly equivalent since the misalignment affects the response of the crystal to different photon energies, but the energy-dependent responses of the attenuators and the detector are not affected. The signal aligned using an energy reference (In K-edge, 27.94 keV) is shown as $M_n'(x + \delta x)[G_1'(E)]$, where a constant shift δx by Eq. 8 corresponding to E = 27.94 keV was applied. Figure 9(e) shows spectral representations of the aligned signal $M_n'(x + \delta x)[G_1'(E)]$, one labeled $S_p(E)[M_n'(x + \delta x)][G_1'(E)][G_1(E)]$ obtained using the original crystal's sensitivity $G_1(E)$, and the other labeled $S_p(E)[M_n'(x + \delta x)][G_1'(E)][G_1'(E)]$ using the corrected spectral sensitivity $G_1'(E) = G_1(E + \delta E)$. The latter is in much better agreement with the original spectrum $S_0(E)$. The corresponding residuals shown in Figure 9(c) remain acceptable except the small problematic low-energy region $E \lesssim 21$ keV where the nominal dispersion deviates from the polynomial fit. Thus, above this energy, the simulations validate the applicability of the derived crystal sensitivity corrections due to pointing and insertion errors.

VII. DATA ANALYSIS

In this section we describe data analysis using images of continuum spectra recorded for two indirectly-driven ICF experiments as examples: shot N220220 was an ex-

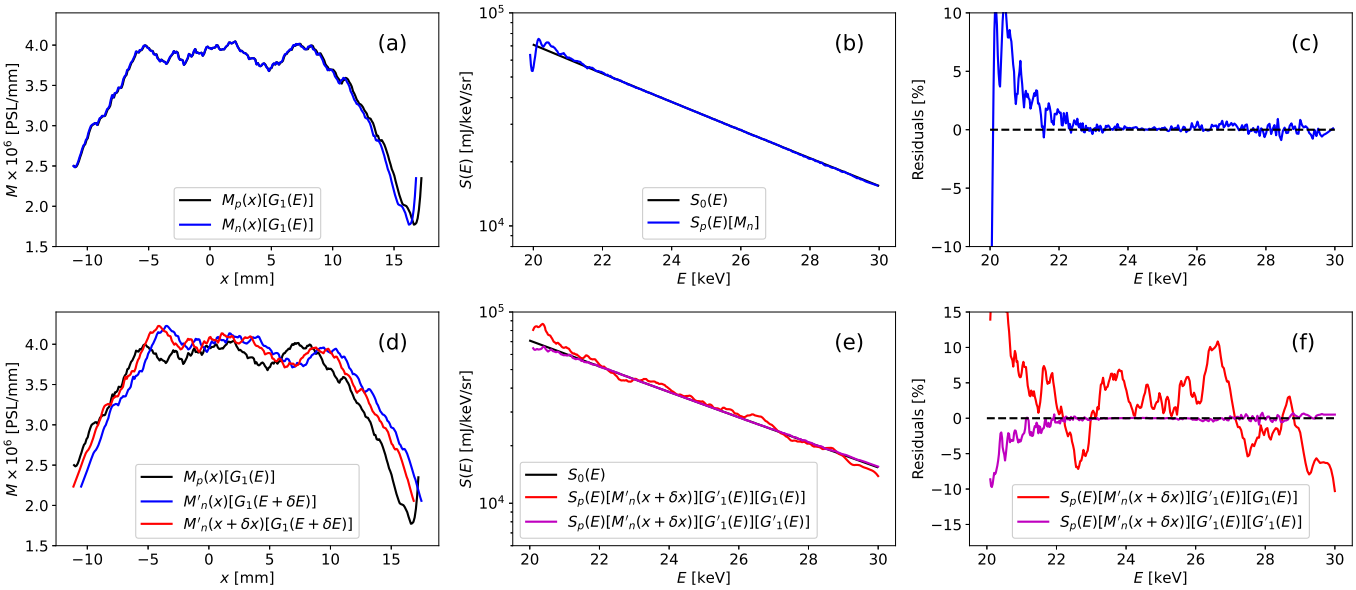

FIG. 9. Results of simulations used to validate the corrections to crystal sensitivity due to pointing and insertion errors: (a-c) Signals recorded by the detector, their recovered spectral representations and residuals to illustrate the errors in using the nominal dispersion assuming that the polynomial fit represents the true dispersion of the spectrometer. (d-f) Signals recorded by the detector, their spectral representations and the residuals to illustrate the applicability of the developed corrections in the worst possible case of spectrometer's pointing error δH = -0.5 mm, and insertion error δL = 2.0 mm. See text for details.

periment using a THD fuel contained in the imploding capsule while the other shot N220919 was using a DT fuel. The latter experiment results in a dramatic increase in x-ray emission and is accompanied by a much higher yield of 14.1 MeV neutrons due to DT fusion reactions. The same crystal calibrated as described in Section III was employed in ConSpec in both experiments using the limiting entrance aperture of 5 mm.

The spectral signal M recorded on the image plate in the THD experiment (shot N220220) is shown in Fig. 10(a). To improve data statistics the image was binned in the spectral direction where image intensities from 8 neighboring pixels are averaged into one pixel. The binning is chosen to not exceed the expected energy resolution of the crystal spectrometer ($\simeq$ 80-200 eV). It is convenient to perform initial image analysis operating with pixel numbers. Index notations i and j are ascribed to enumerate the pixels in the spectral and in the imaging directions of the spectrometer, respectively. The image is centered on the bright x-ray emission spectrum from the reaction's hot spot. The hot spot's emission is accompanied by the relatively weak diagonal streaks of intensity (side lobes) due to bremsstrahlung radiation from the Au-lined high-Z hohlraum. The separation between the side lobes and the hot spot spectrum increases at lower energies due to increasing magnification of the spectrometer.

Figures 10(b,c) show vertical slices of the binned image corresponding to two distinct locations along the spectrum. These locations are indicated on Fig. 10(a) by the dashed vertical lines. The first profile selected from the high-energy portion of the spectrum is shown in Fig. 10(b) with the black curve. The baseline of the profile represents the background of the image (a relatively small portion of the signal for the THD shot). This baseline was obtained by linear interpolation of the averaged signal values at the tails of the profile (averaged over 40 pixels). The shape of the profile suggests that the tails of the side lobes overlap with those of the hot spot signal. In order to extract the hot spot signal the profile was fit to a sum of three Lorentzian curves. The fitted Lorentzian curves are shown with red, magenta and blue lines. The sum of the Lorentzian curves is shown with a green line. The hot spot signal was extracted by subtraction of the baseline along with the two Lorentzian fits of the side lobes from the raw data and summing the result in the range indicated by the vertical dashed lines. This range corresponds to the width of the aperture on the Amptek detector used in measurements of the crystal's sensitivity (4.7 mm). The second profile selected from the lower-energy portion of the spectrum is shown in Fig. 10(c) with black curve. The profile is dominated by the hot spot signal while the side lobes represent a negligible contribution. The fit using 3 Lorentzian shapes failed for this particular profile and other profiles at horizontal positions i > 89. Therefore, these profiles were fit using a single Lorentzian curve. The hot spot signal was extracted by subtracting the baseline from the raw data for each profile and summing result in the same region represented by the two vertical

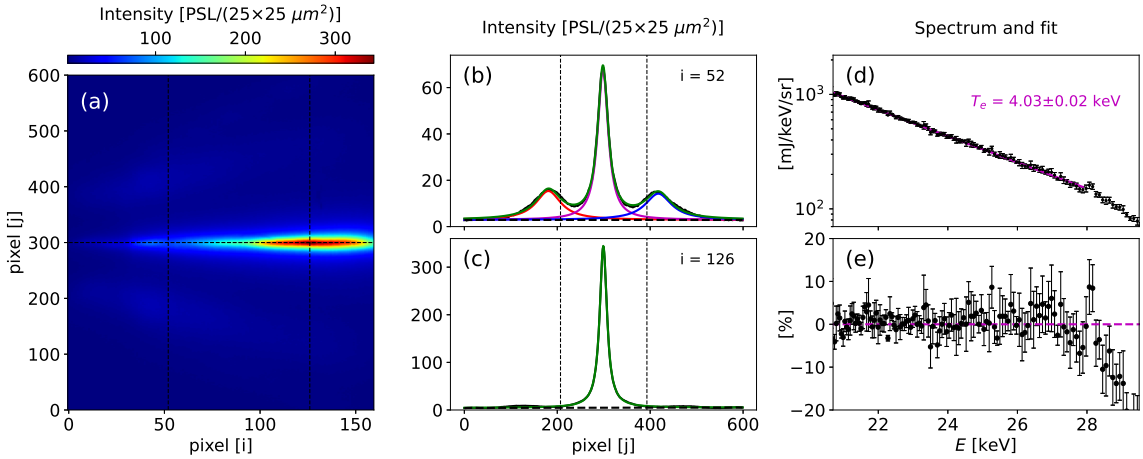

FIG. 10. Data analysis procedure for an ICF experiment N220220 using THD fuel: (a) Working region on the image plate including the x-ray spectrum, the side lobes due to emission from the hohlraum and the background. The original image is 8×1 binned/averaged (8 pixels to 1 in the spectral direction). Photon energies decrease from left to right. (b,c) Selected vertical slices of the image (at locations indicated by the dashed vertical lines in (a)) illustrating data analysis procedure: (b) fitting the profile with 3 Lorentzian peaks, subtracting the baseline along with the fitted side lobes and summing the resulting signal in the range indicated by the vertical dashed lines; (c) fitting the profile with a single Lorentzian peak (the side lobes are neglected), subtracting the baseline and summing the resulting signal in the same range. (d) X-ray spectrum calculated from the extracted signal using the first-order spectrometer response (circles and errorbars) and a fit to Eq. 1 performed in the range 20.7-27.9 keV (magenta line) showing the extracted T_e. (e) Fit residuals; $\tilde{\chi}^2 = 1.0$ of the fit indicates good statistical match of the measured signal to the fit function.

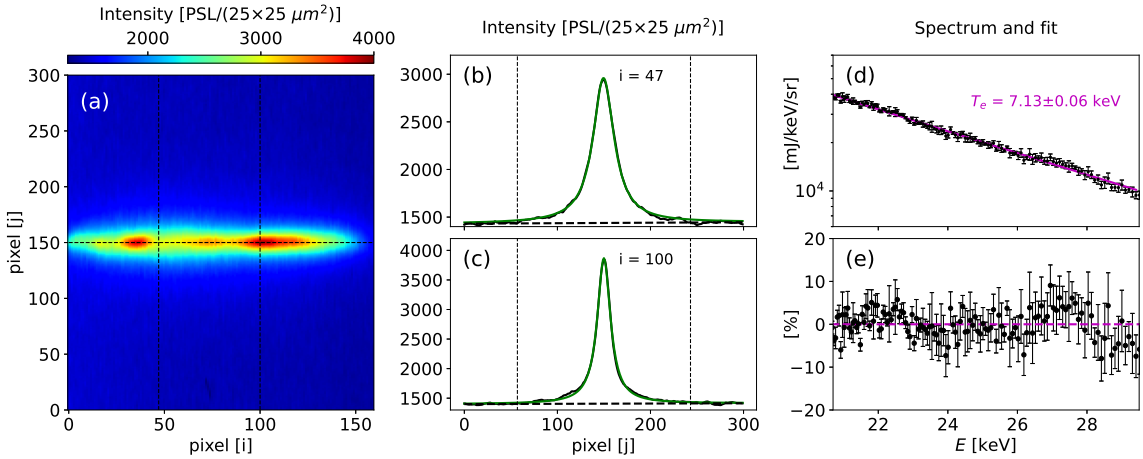

FIG. 11. Data analysis procedure for an ICF experiment N220919 using DT fuel: (a) Working region on the image plate including the x-ray spectrum and the surrounding high-level (≃ 1400 PSL average) background due to neutron yield. The original image is 8×1 binned/averaged (8 pixels to 1 in the spectral direction). Photon energies decrease from left to right. The hohlraum emission is not resolved. (b,c) Selected vertical slices of the image (at locations indicated by the dashed vertical lines in (a)) illustrating data analysis procedure: fitting the profile with a single Lorentzian peak, subtracting the baseline and summing the resulting signal in the range indicated by the vertical dashed lines. (d) X-ray spectrum calculated from the extracted signal using the first-order spectrometer response (circles and errorbars) and a fit to Eq. 1 performed in the range 20.7-29.5 keV (magenta line) showing the extracted T_e. (e) Fit residuals; $\tilde{\chi}^2 = 1.2$ of the fit indicates an observable mismatch of the measured signal to the fit function.

dashed lines. In this case, the fit with Lorentzian curve is performed only for testing purposes (e.g., to monitor the spatial extent/width of the hot spot signal). Summing the fitted Lorentian profiles of the hot spot signal instead of summing the baseline-subtracted signal itself was considered as an alternative, but such procedure resulted in additional distortions of the spectral shape, which could be explained by the empirical nature of the approximation. Depending on variations in the microstructure of the HAPG crystal the profile of the reflected x rays can

deviate from the Lorentzian shape and from any other empirical shape chosen for the analysis. At the same time, the approximation of the side lobes with an empirical shape for the purpose of extracting the primary signal is acceptable as long as their contribution to the signal is small.

In this experiment a 15 μm-thick In attenuator placed at the nose cone LRU served as an energy reference. The rapid reduction of the image intensity at i = 33 is due to the In absorption K-edge E_{In} = 27.94 keV, which corresponds to x_{In} = -7.01 mm according to the polynomial approximation of the spectrometer's dispersion (Fig. 4). The x scale was calibrated by assigning this value to the K-edge position. The photon energy scale was then assigned to the calibrated x scale using the spectrometer's dispersion. The spectrum calculated using the first order spectrometer response is shown in Fig. 10(d).

$$S(E) = \frac{M(E)}{\tilde{G}_1(E)} \tag{9}$$

The errorbars (± standard deviation) represent the uncertainties in determination of the crystal's sensitivity G_1 combined with the noise extracted by sampling the tails of the signal profiles. The respective relative uncertainties of the two contributions were added in quadrature. We note that the noise originating from the background represents a relatively small contribution (< 1%). A fit to the spectral shape defined by Eq. 1 ($\tau = 0$) is shown in magenta. It was performed in the range of energies 20.7-27.9 keV. Thus the fit did not include energies above the In K-edge because of an incomplete compensation of the reduced signal with tabulated attenuation of In. This is attributed to signal broadening caused by the finite spectral resolution of the crystal. We note that this resolution is not an exact match to the resolution of the Amptek detector used in the calibration. Thus, complete compensation of narrow-bandwidth spectral features (e.g. characteristic lines or the absorption edge) is not expected. Figure 10(e) shows the fit residuals. To test the statistical match between the measured spectrum and the fit to Eq. 1 we use the reduced χ^2, $\tilde{\chi}^2 = \chi^2/\nu$, where $\nu = n-m$ is the number of degrees of freedom, i.e. the number of observations n minus the number of fitted parameters m (m = 2 in our case). For the fit shown in Fig. 10(d) $\tilde{\chi}^2 \simeq 1.0$, which indicates a good statistical match.

The spectral signal M recorded on the image plate in the DT experiment (shot N220919) is shown in Fig. 11(a). The image was binned similarly to the previous case. The image is centered on the bright x-ray emission spectrum from the reaction's hot spot. The side lobes due to hohlraum emission are not present on the image. This could be explained by the very low level of the detected hohlraum's emission compared to the level of neutron-induced background and the fact that the dynamic range of detection is limited by noise. Assuming that the hohlraum emission level is about the same in the two experiments (1.9 MJ and 2.05 MJ laser energy delivered in the THD and DT experiments, respectively) the maximum hohlraum emission on N220220 is at about 1 % of the background baseline on N220919, which is comparable to the noise level. Due to the absence of the side lobes the size of the working region of the image in the vertical direction was reduced to 300 pixels (7.5 mm). Figures 11(b,c) show vertical slices of the binned image corresponding to two distinct locations along the spectrum. These locations are indicated on Fig. 11(a) by the dashed vertical lines. The profiles are shown with black lines while the Lorentzian fits to these profiles are shown with green lines. The baselines (dashed lines) were obtained by linear interpolation of the averaged signal values at the tails of the profile (averaged over 40 pixels). For each vertical profile the hot spot signal was extracted by subtracting the baseline from the raw data and summing result in the region represented by the two vertical dashed lines (the size of the region corresponding to the size of the aperture on the Amptek detector). In this experiment ConSpec was configured using only Ti attenuators. The use of the absorption edge attenuators was avoided to preserve the entire spectral range of the instrument. The position of the reference energy was chosen to be the same as in the previous experiment upon alignment of the respective images using locations of the alignment holes in the IPs, which ensure identical placement of the IPs in the spectrometer. The reference energy, however, can shift with respect to this nominal location due to the alignment errors as described in Section VI. This shift is dominated by the spectrometer's pointing error according to Eq. 8. This possible shift was systematically varied. For each value of the shift within the confidence interval of ± 0.5 mm the data analysis described above was repeated starting from assignment of the energy scale to the extracted signal followed by calculation of the spectrum according to Eq. 9 and fitting to the spectral form of Eq. 1. The fitting was performed upon application of systematically varied corrections to the spectrometer's sensitivity by Eq. 6. The procedure revealed that the best fit was obtained using the reference energy location being off the location assigned initially by only 75 μm, which is comparable to the intrinsic resolution of the image plate. In the final fit the correction to the energy scale of the sensitivity was set to zero. The resulting spectrum and the fit are shown in Fig. 11(d) along with the extracted T_e =7.13 keV, which increases substantially compared to the value for the THD shot. The fit residuals shown Fig. 11(e) reveal deviations from the nominal spectral shape, which are slightly greater than the error bars. For this fit, $\tilde{\chi}^2$ =1.2, which suggests that the extracted spectral data deviates from Eq. 1. The errorbars (± standard deviation) were obtained similarly to the previous case: the uncertainties in determination of the crystal's sensitivity G_1 were combined in quadrature with the noise extracted from the tails of the signal profiles. We note that for the DT shot the signal noise originating from the background fluctuations remains small (relative uncertainty of < 1%).

VIII. NEUTRON-INDUCED BACKGROUND

The background was explored experimentally using additional arrangements in the spectrometer's body during ICF experiments and theoretically using GEANT4 simulations where 14.1 MeV monoenergetic neutrons originating at the nominal target location were propagated through an arrangement of hardware approximating the spectrometer. In a series of ICF experiments a new line-of-sight (LoS) shield was placed along the DIM axis and an additional IP placed at a distance behind that shield. This arrangement shown in Fig. 12(a) formed a separate testing branch of the instrument while the primary spectroscopy branch was unaffected.

One version of the new LoS shield included blocks of B_4C with combined thickness of 17 cm followed by a block of W with thickness 6.75 cm. In the second version of the new LoS shield W was replaced with additional blocks of B_4C. A testing step down filter was a stripe of 5 mm-thick Cu combined with 0.5 mm-thick Al. It was placed directly in front of the IP (the IP was shielded with a layer of black Kapton). Upon fielding these configurations on ICF experiments the signals observed on IP images were studied and compared with results of GEANT4 simulations. One of such experimental images from shot N211009 is shown in Fig. 12(b). The LoS shield configurations were included in the simulations while the actual spectrometer enclosure (asymmetric, Fig. 1(a)) was approximated with four Al plates arranged symmetrically with respect to the LoS.

A GEANT4 simulated image is shown in Fig. 12(c). The image contrast in the simulation formed with the combined contributions of neutrons, neutron-induced x rays and neutron-induced electrons is in approximate agreement with the experiment. We note that the actual PSL values in the simulated image multiplied by the neutron yield of the experiment 6.2×10^{16} and normalized to the resolution element (pixel area) exceed the experimental result by about factor of 4. This can be explained by the approximation of the spectrometer enclosure with the Al plates. It does not take into account hardware upstream of the LoS (e.g., crystal and the crystal limiting aperture), which can scatter a substantial fraction of neutrons. We also note that in a separate simulation without the Al plates the attenuation contrast due to the testing step down filter was absent. The results are consistent with a picture where the prompt radiation emitted from the target is well attenuated by the LoS shield, however the background is still high due to secondary radiations originated elsewhere in the spectrometer body. GEANT4 simulations reporducing the experimental images revealed that the primary source of signal contrast was due to the neutron-induced electrons. In this regard, we were unable to confirm performance of the LoS shields experimentally. The central portion of the IP directly shielded with the B_4C+W combination showed about the same signal level as that of a separate simulation using B_4C only shield. No well-defined boundary

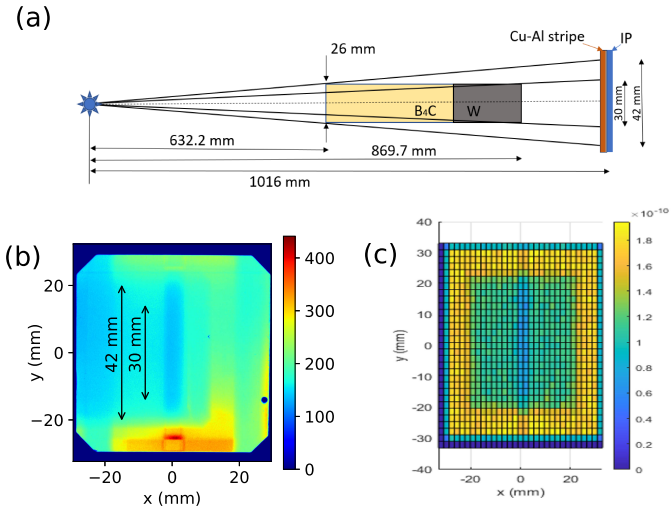

FIG. 12. (a) Schematics of the testing branch of the spectrometer along the DIM axis. The prompt radiation is blocked by the new LoS shield which contains 17 cm of B_4C and 7 mm of W. The dimensions marked on the IP correspond to the sizes of the point source projections of the shield boundaries. A Cu-Al stripe is placed directly on IP to test its background attenuation. (b) The image recorded for shot N211009 (neutron yield 6.2 $\times10^{16}$). The units on the colorbar are PSL/pixel (25×25 μm^2). The dimensions marked with arrows are the same as in (a). Contrast corresponding to the W block boundary (30 mm) is not observed. (c) GEANT4 simulated IP image where the image contrast is formed with the combined contributions of neutrons, neutron-induced electrons and neutron-induced x rays. The units on the colorbar are in PSL/pixel (2×2 mm^2) per neutron.

corresponding to projection of the W block boundaries were observed on the IP, which is consistent with a signal where the dominant contribution is due to secondaries. In a series of additional GEANT4 simulations using thick W plates placed around the IP revealed reduction in the background levels in the side-shielded region. Thus, using high-Z collimators for the detector could be a valid strategy to reduce the background in x-ray diagnostics operating in the high-neutron-yield environment.

IX. DISCUSSION

ConSpec-measured x-ray continuum spectra are substantially different for the two experiments. Table III shows the apparent electron temperatures, levels of spectral emission at selected energies as well as the average ion temperatures T_i^{DT} reported by nTOF (neutron time-of-flight) diagnostic at NIF. We note that the apparent electron temperature is in good agreement with the ion temperature for the THD shot while the ion temperature for the DT shot substantially exceeds the apparent T_e. This could be related to a very different spatial distribution of the neutron-emitting volume compared to that of the x-ray emission. The discrepancy could

TABLE III. The extracted apparent T_e, the averaged T_i^{DT} measured with nTOF detectors and the levels of spectral emission at selected energies.

Shot	T_e [keV]	T_i^{DT} [keV]	$S(E)$ [J/keV/sr]		
			21 keV	23 keV	28 keV
N220220	4.03(0.02)	4.04(0.13)	0.96	0.56	0.15
N220919	7.13(0.06)	10.1(0.22)	37.7	27.5	12.6

be explained by a substantial fraction of relatively cold emitting plasma surrounding the neutron-producing hot spot. The levels of the spectral emission are also dramatically different for the two experiments. The levels corresponding to the DT shot are exceeding those of the THD shot by $\simeq$ 40-80 times, which illustrates the two different regimes of DT reaction.

The residuals from the fit to the expected spectral shape (Eq.1) presented in Fig. 10(e) and Fig. 11(e) show an agreement to within $\pm$ 10%. For the THD shot the residuals in the measurement range 20.7-29.5 keV appear to be of random character considering the measurement uncertainties $\simeq \pm$ 5% (r.m.s.). However, for the DT shot non-monotonic residuals slightly exceeding the estimated measurement uncertainties are observed. The wavy appearance of the residuals indicates that any other monotonic function, which could be expected from a theoretical perspective (e.g., absence of characteristic emission/absorption features in the studied spectral range) is unlikely to match the measured spectrum. In this regard, we summarize possible systematic uncertainties of the measurement method. Our analysis rules out errors in the spectrometer sensitivity due to spectrometer misalignment, influence of the higher crystal reflection orders and that of the neutron-induced background. The spectrometer sensitivity was measured off-line in a detector-independent fashion. The related measurement uncertainties were quantified. The remaining possibility is a change in the crystal sensitivity resulting from its deterioration due to the harsh radiation environment in the target chamber (the same HAPG crystal was used on many high yield DT shots). A repeated off-line crystal characterization is not straightforward since the crystal spectrometer remains highly activated for weeks after the shot. To address the issue, future work may include fielding the spectrometer on a calibration shot where the crystal response is verified using a predictable x-ray spectrum.

X. CONCLUSIONS

In summary, we have developed a methodology for measuring time-averaged x-ray continuum spectra of ICF implosions including those accompanied by high yields of 14.1 keV DT neutrons producing high levels of background recorded using time-averaging detectors such as image plates. The method relies on the use of ConSpec, a sagittally-focusing high-throughput spectrometer using a highly annealed pyrolytic graphite crystal, which measures spectra in $\simeq$ 20-30 keV range. The sensitivity of the HAPG crystal measured in an off-line x-ray laboratory setting in our prior study was revised. The error analysis was expanded to include the accuracy of the off-line measurements in evaluation of the crystal's sensitivity, the effect of the neutron-induced background as well as influence of possible errors in alignment of the instrument to the ICF target.

Applications of the improved methodology were demonstrated for two ICF experiments at the National Ignition Facility, an implosion using THD fuel with a relatively low yield (4.33×10^{14}) of 14.1 MeV neutrons and a DT implosion with a high neutron yield of 3.82×10^{17}. The measured continuum spectra demonstrate two very different regimes of ICF where the logarithmic slopes of the spectra (the apparent electron temperatures) are determined as well as the levels of x-ray emission in absolute units. In both cases, the shape of the measured spectrum agrees with the exponentially decaying spectral shape of bremsstrahlung emission to within $\pm$ 10%. In the case of high-yield DT experiment non-monotonic deviations slightly exceeding the measurement uncertainties are observed. The origin of these deviations are likely related to unaccounted systematic errors such as changes in the crystal response induced upon experiencing the harsh radiation environment of implosions in the NIF target chamber.

XI. ACKNOWLEDGMENTS

This work was performed under the auspices of the U.S. Department of Energy by Lawrence Livermore National Laboratory under Contract DE-AC52-07NA27344.

XII. DATA AVAILABILITY

The data that support the findings of this study are available from the corresponding author upon reasonable request.

[1]D. Cao, R. C. Shah, S. P. Regan, R. Epstein, I. V. Igumenshchev, V. Gopalaswamy, A. R. Christopherson, W. Theobald, P. B. Radha, and V. N. Goncharov, Phys. Plasmas **26**, 082709 (2019).

[2]G. Kagan, O. Landen, D. Svyatskiy, H. Sio, N. Kabadi, R. Simpson, M. Gatu Johnson, J. Frenje, R. Petrasso, R. Shah, T. Joshi, P. Hakel, T. Weber, H. Rinderknecht, D. Thorn, M. Schneider, D. Bradley, and J. Kilkenny, Contributions to Plasma Physics **59**, 181 (2019).

[3]L. C. Jarrott, L. R. Benedetti, H. Chen, N. Izumi, S. F. Khan, T. Ma, S. R. Nagel, O. L. Landen, A. Pak, P. K. Patel, M. Schneider, and H. A. Scott, Rev. Sci. Instrum. **87** (2016), 11E534.

[4]L. C. Jarrott, B. Bachmann, T. Ma, L. R. Benedetti, F. E. Field, E. P. Hartouni, R. Hatarik, N. Izumi, S. F. Khan, O. L. Landen, S. R. Nagel, R. Nora, A. Pak, J. L. Peterson, M. B. Schneider, P. T. Springer, and P. K. Patel, Phys. Rev. Lett. **121**, 085001 (2018).

[5]H. Scott and S. Hansen, High Energy Density Physics **6**, 39 (2010).
[6]B. Bachmann, J. E. Ralph, A. B. Zylstra, S. A. MacLaren, T. Döppner, D. O. Gericke, G. W. Collins, O. A. Hurricane, T. Ma, J. R. Rygg, H. A. Scott, S. A. Yi, and P. K. Patel, Phys. Rev. E **101**, 033205 (2020).
[7]H. Abu-Shawareb et al., Phys. Rev. Lett. **129**, 075001 (2022).
[8]A. B. Zylstra et al., Phys. Rev. E **106**, 025202 (2022).
[9]A. L. Kritcher et al., Phys. Rev. E **106**, 025201 (2022).
[10]D. B. Thorn, A. MacPhee, J. Ayers, J. Galbraith, C. M. Hardy, N. Izumi, D. K. Bradley, L. A. Pickworth, B. Bachmann, B. Kozioziemski, O. Landen, D. Clark, M. B. Schneider, K. W. Hill, M. Bitter, S. Nagel, P. M. Bell, S. Person, H. Y. Khater, C. Smith, and J. Kilkenny, Proc. SPIE - Int. Soc. Opt. Eng. **10390**, 22 (2017).
[11]M. MacDonald, B. Kozioziemski, A. MacPhee, M. Schneider, J. Ayers, and D. Thorn, J. Instrum. **14**, P12009 (2019).
[12]T. A. Hall, J. Phys. E: Sci. Instrum. **17**, 110 (1984).
[13]A. G. MacPhee, P. M. Bell, D. Boyle, A. C. Carpenter, L. Claus, M. Dayton, J. Dean, A. K. L. Dymoke-Bradshaw, C. Durand, B. Funsten, A. Garafalo, B. P. Golick, J. D. Hares, J. Hill, J. M. Kehl, S. F. Khan, J. D. Kilkenny, M. J. MacDonald, D. Maheshwari, I. J. Mccubbin, S. R. Nagel, P. R. Nyholm, N. E. Palmer, R. B. Petre, M. Sanchez, M. B. Schneider, M. O. Schoelmerich, S. Stoupin, and A. Welton, Rev. Sci. Instrum. **93**, 083519 (2022).
[14]B. J. Kozioziemski, J. Ayers, P. Bell, D. K. Bradley, M.-A. Descalle, S. Hau-Riege, T. J. McCarville, T. Pardini, L. A. Pickworth, J. K. Vogel, J. Stone, J. Robinson, D. J. Ampleford, C. R. Ball, C. J. Bourdon, J. R. Fein, M. Wu, A. Ames, R. Bruni, and S. Romaine, Review of Scientific Instruments **89** (2018).
[15]B. MacGowan, O. Landen, D. Casey, C. Young, D. Callahan, E. Hartouni, R. Hatarik, M. Hohenberger, T. Ma, D. Mariscal, A. Moore, R. Nora, H. Rinderknecht, D. Schlossberg, and B. Van Wonterghem, High Energy Density Physics **40**, 100944 (2021).
[16]R. Templer, Nucl. Instrum. Methods Phys. Res. A **300**, 357 (1991).
[17]B. R. Maddox, H. S. Park, B. A. Remington, N. Izumi, S. Chen, C. Chen, G. Kimminau, Z. Ali, M. J. Haugh, and Q. Ma, Rev. Sci. Instrum. **82**, 023111 (2011).
[18]M. J. Rosenberg, D. B. Thorn, N. Izumi, D. Williams, M. Rowland, G. Torres, M. Haugh, P. Hillyard, N. Adelman, T. Schuler, M. A. Barrios, J. P. Holder, M. B. Schneider, K. B. Fournier, D. K. Bradley, and S. P. Regan, Rev. Sci. Instrum. **90**, 013506 (2019).
[19]S. C. Burkhart, E. Bliss, P. D. Nicola, D. Kalantar, R. Lowe-Webb, T. McCarville, D. Nelson, T. Salmon, T. Schindler, J. Villanueva, and K. Wilhelmsen, Appl. Opt. **50**, 1136 (2011).